



Hyperspectral Microwave Sensors—Advantages and Limitations

Christian D. Kummerow , Joseph C. Poczatek, Scott Almond, Wesley Berg, Olivia Jarrett, Andrew Jones , Michael Kantner, and Chia-Pang Kuo

Abstract—Temperature and humidity soundings form the bedrock of modern data assimilation due to their ability to directly constrain the atmospheric state variables. Because of their ability to penetrate clouds and work in all weather conditions, microwave sounders have very large impacts on constraining numerical weather prediction models. Recent advancements in integrated microwave assembly, space-grade high speed analog to digital converters, gigabit-per-second data interconnects, and field programmable gate arrays have enabled a transition from traditional analog detector-based demodulators to digitally channelized systems that allow for hyperspectral, or fine spectral resolution microwave sounders to be viable replacements to the current operational instruments. This article demonstrates that retrievals of temperature and moisture soundings can be improved by as much as 50% when 60–80 appropriately chosen pseudochannels are employed. While the current simulations were limited to cloud free oceans, perhaps even greater benefits can be realized over land and cloud conditions where additional channels can help constrain the surface and clouds. The article also demonstrated the advantages of hyperspectral sensors as a way to detect radio frequency interference in the few Kelvin range, as well as its ability to improve intercalibration efforts due to its ability to match frequency response functions of target sensors.

Index Terms—, Data assimilation, hyperspectral, hyperspectral microwave sounders, Microwave Reference Intercalibration Radiometer (MIRER), millimeter wave, moisture, radio frequency interference, retrieval, sounding, temperature, water vapor.

I. INTRODUCTION

TEMPERATURE and humidity soundings form the bedrock of modern data assimilation due to their ability to directly constrain the atmospheric state variables. The primary sources of global sounding data are satellite infrared (IR) and passive microwave sensors, although radio occultation [1] has also had success in constraining numerical models. While IR sensors dominated the very early instrument suites, and have very good

vertical resolution, they are limited to cloud-free scenes. To overcome this limitation, microwave sensors were deployed. While their weighting functions and subsequent vertical resolution are much broader than their IR counterparts, their ability to penetrate clouds and work in all weather conditions make them perhaps the most useful instruments for constraining numerical weather prediction (NWP) models (e.g., [2]).

Space-based microwave radiometry has been shaped by multiple technological advancements, both in the fidelity of the science collected as well as instrument architecture. While a similar capability to temperature retrievals using CO₂ absorption by IR sounders was known to exist in the 50–60 GHz using Oxygen absorption, thus bypassing the clear sky requirement, mm wave solutions were hindered initially by poor spatial resolution and sensitivity. In 1978, NASA launched the Microwave Sounding Unit (MSU) on the Television and InfraRed Observation Satellite (TIROS-N) satellite; it was the world's first operational microwave temperature sounder. The charter for the TIROS-N mission was to demonstrate the usefulness of satellite weather imagery, focusing on simplicity. To that end, the MSU produced only 4 channels in the 50 GHz window and leveraged a Dicke switching architecture for calibration. Nadir resolution was 110 km. Despite the relatively modest feature set compared with modern offerings, MSUs flew on subsequent missions for over two decades.

In 1979, the Department of Defense launched their own weather solution in the form of the Special Sensor Microwave – Temperature (SSM/T) instrument. The SSM/T instrument had 7 channels in the 50–60 GHz range. Five additional channels from 90 to 183 were contained on a separate instrument called the SSM/T-2. The three instruments (SSM/T, SSM/T-2, and SSM/I (having channels between 18.7 and 85.5 GHz) were ultimately combined to produce the conically scanning SSMIS instrument with 24 channels. In parallel, the MSU and Stratospheric Sounding Unit were combined to form the Advanced Microwave Sounding Unit (AMSU) in the NASA/NOAA development line. There were two variants: AMSU-A for channels 89 GHz and below, and AMSU-B for 89 GHz and above. AMSU improved the spatial resolution by more than a factor of two over its predecessors while also improving sensitivity. This allowed better resolution of thermal boundaries in the atmosphere. AMSU-A and AMSU-B would later be merged to form the advanced technology microwave sounder (ATMS).

SSMIS first launched on defense meteorological satellite program flight 16 in 2003, and ATMS launched on Suomi National

Manuscript received August 23, 2021; revised November 6, 2021; accepted November 24, 2021. Date of publication December 9, 2021; date of current version January 12, 2022. The work was supported by NOAA under Grant 1332KP20CNEEP0069. (Corresponding author: Christian D. Kummerow.)

Christian D. Kummerow, Wesley Berg, Andrew Jones, and Chia-Pang Kuo are with the Colorado State University, Fort Collins, CO 80523-1375 USA (e-mail: kummerow@atmos.colostate.edu; wesley.berg@colostate.edu; andrew.s.jones@colostate.edu; chia-pang.kuo@colostate.edu).

Joseph C. Poczatek, Scott Almond, Olivia Jarrett, and Michael Kantner are with the Northrop Grumman Corporation, Falls Church, VA 22042 USA (e-mail: joseph.poczatek@ngc.com; scott.almond@ngc.com; olivia.jarrett@ngc.com; michael.kantner@ngc.com).

Digital Object Identifier 10.1109/JSTARS.2021.3133382

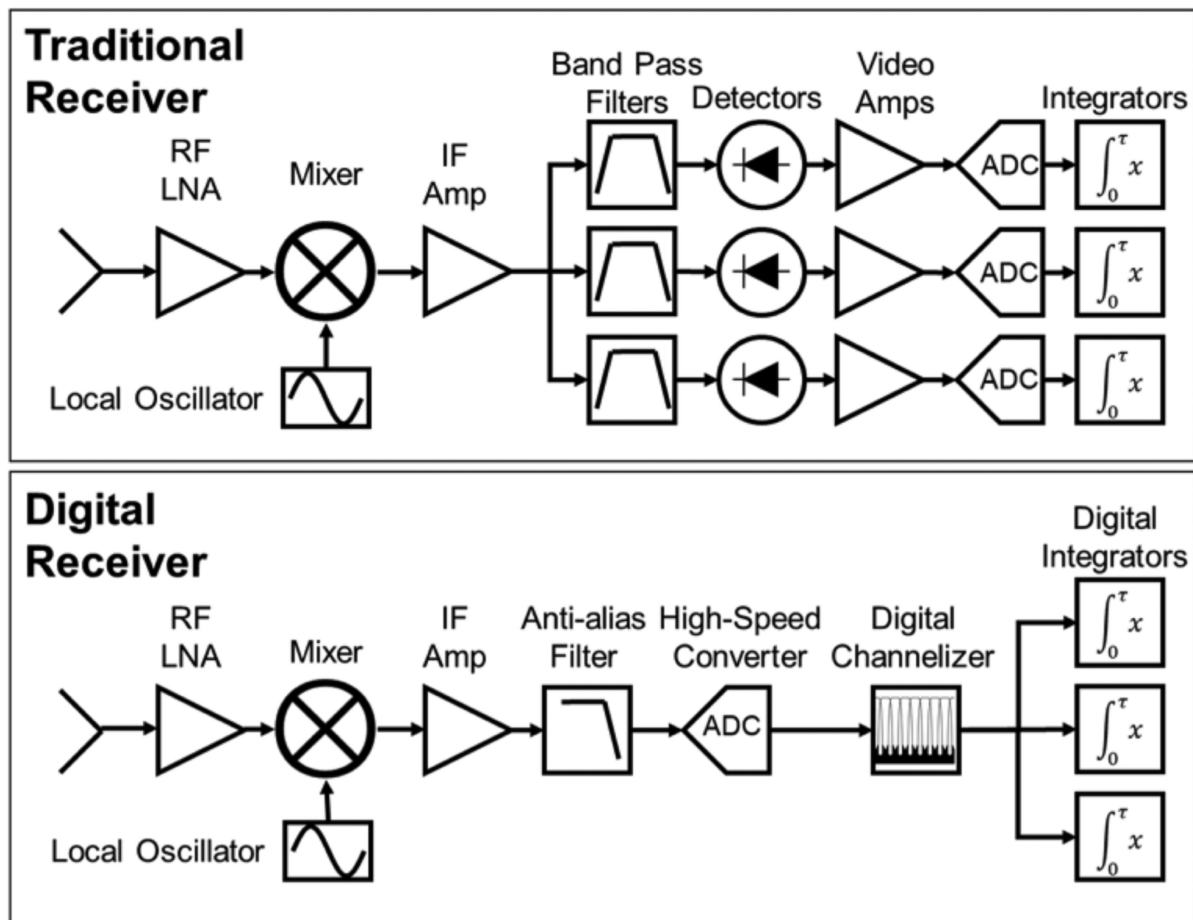


Fig. 1. Comparison of traditional receiver channelization architecture and the digital alternative.

Polar-orbiting Partnership (SNPP) in 2011. SSMIS leverages square law detectors to charge-and-dump capacitors at a rate in the single kHz regime. This is overcome by ATMS, designed a decade later, with analog to digital converters (ADCs) running in the 100 kHz range, enabling greater operational flexibility and reducing analog artifacts, yet still relying on square-law detectors. It is also worth noting that both SSMIS and ATMS use external radiometric calibration to better characterize radiometer noise contributions versus Dicke switching used in earlier generation instruments. A modern approach to digital sampling could leverage space-grade GHz ADCs, unlocking the potential for radio frequency interference (RFI) detection and ripple correction in the process. High rate ADCs and field programmable gate arrays (FPGAs) also allow for digital channel formation. While ATMS uses a surface acoustic wave (SAW) filter, and soil moisture active passive (SMAP) employs a digital filter bank [the first in the world to mitigate RFI using on-board digital signal processing (DSP)] for this purpose, it is reasonable to assume full digital filtering will become the baseline for fine bandwidth channels in future architectures.

Compared to IR absorption bands, the bands in the passive microwave are few—an Oxygen complex in the 54–60 GHz range, an additional line at 118 GHz for temperature sounding and water vapor absorption lines at 22.235 and 183.31 GHz. The absorption lines are fairly broad except for the 54–60 GHz

Oxygen complex. Even with relatively broad lines, there are advantages to using finer spectral resolution as pointed out in previous publications [3]–[6]. The following sections describe a fully defined sensor, the Microwave Reference Intercalibration Radiometer (MIRER), along with simulations intended to assess the abilities of MIRER-like sensors to improve current state of the art microwave retrievals of temperature and humidity, as well as aid in the detection of radio frequency interference (RFI) and improve intersensory calibration that becomes critical for the construction of climate data records.

II. MICROWAVE REFERENCE INTERCALIBRATION RADIOMETER

Recent advancements in integrated microwave assembly (IMA), space-grade high speed ADCs, gigabit-per-second data interconnects, and FPGAs have enabled a transition from traditional analog detector-based demodulators to digitally channelized systems.

The key difference between a traditional receiver architecture and the digital approach is illustrated in Fig. 1. Traditional architectures require separate down-conversion and filtering stages for each band of interest while a digital approach leverages wideband ADCs and FPGAs to digitize and channelize a broad spectrum with a single receiver chain. This is particularly advantageous for instruments supporting frequency bands with many

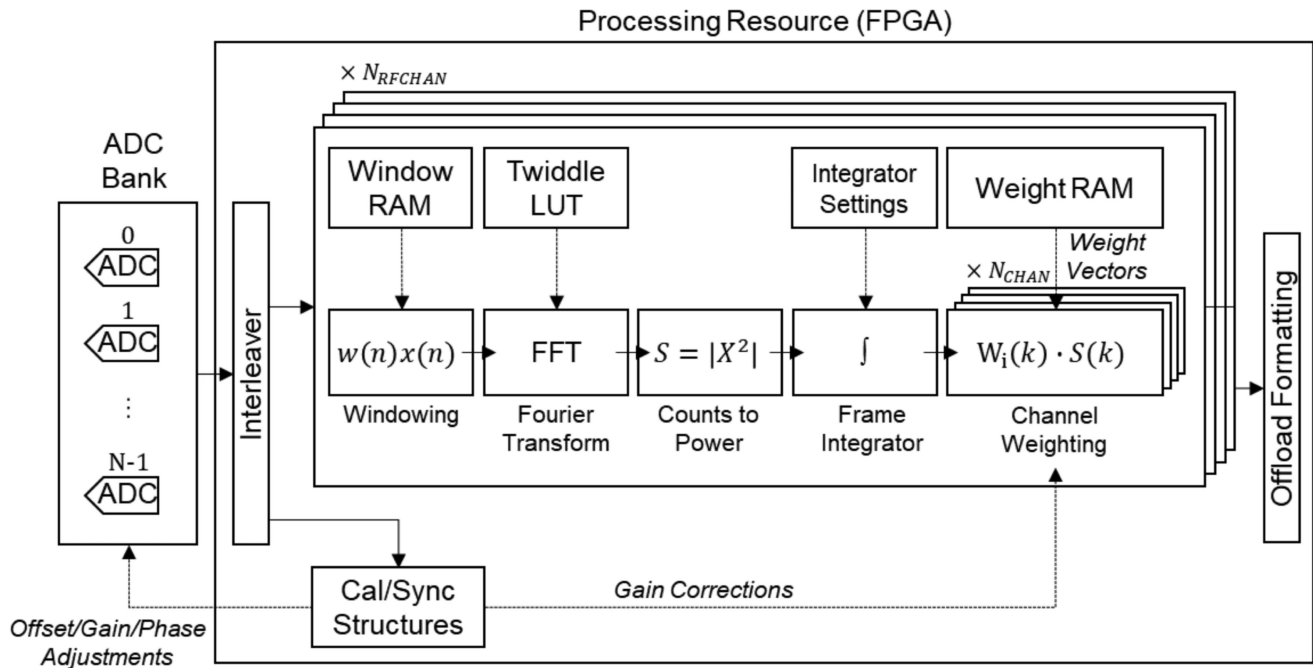


Fig. 2. FFT spectrometer reference design leveraging multiple analogs to digital converters and processing chains.

channels; including future digital successors of ATMS that will cover CH 10 – 15 (the 57.2933 GHz line) without the need for a complex SAW filter assembly.

First introduced by SMAP, space-based digital radiometer back-ends sample wide RF bandwidths and form channels using multirate digital signal processing techniques. While SMAP leverages 96 Msp/s ADCs [3], multigigasample-per-second data converters for space applications are now commercially available. Texas Instruments has released the ADC12DJ3200 capable of sampling at 6.4 Gsp/s with a 3 dB analog input bandwidth of 8 GHz. Networking and data center applications have driven the advancement of high speed serial (HSS) transceivers in low-power packages. Lane rates exceeding 10 Gbps are now possible with space-grade FPGAs containing multiple transceivers. The Xilinx Kintex UltraScale KU060 has 32 HSS transceivers with space-grade variants supporting up to 400 Gbps combined data transfer throughput. This is sufficient to support multiple high speed ADCs on a single circuit card.

Digital processing of wideband data requires a backend capable of performing billions of mathematical operations per second. Until recently, the throughput required for multi-GHz systems could only be achieved through application specific integrated circuits. As reprogrammable FPGAs suitable for a space environment evolved, flexible digital channelization architectures were made possible at a fraction of the cost and development time. There are several approaches for developing multichannel digital radiometers, including: tune-filter-decimation pipelines, polyphase filterbanks, and fast Fourier transform (FFT) spectrometers. Tune-filter-decimate pipelines are the digital equivalent of traditional RF mixing and filtering stages, but multiple channels can be formed without suffering RF splitting loss. Polyphase filterbanks allow efficient frequency selection and filtering of tens of bands through a combination

of finite-duration impulse response filters and FFT stages. As demonstrated by SMAP, multichannel digital radiometers provide additional protection against radio frequency interference through real-time detection algorithms. FFT spectrometers represent the current state of the art as they enable transformation of time series signals into thousands of independent hyperspectral channels.

Fig. 2 shows a FFT spectrometer reference architecture suitable for MW hyperspectral sounding. In this architecture, multiple high-speed analogs to digital converters are integrated into a single circuit card assembly (CCA) with a FPGA processing resource. Sampled data from each converter is transmitted to the processing resource via multiple HSS transceiver pairs. Link protocols that enable deterministic data latency such as JESD204B/C ensure data from each converter can be time aligned for consistent interleaving. Independent Intermediate Frequency (IF) channels or interleaved data streams are processed with a windowing function. A Blackman–Harris window is a suitable choice for most applications as it reduces spectral leakage (interchannel interference) without greatly reducing the power of the processed signal. After windowing, time series data is converted to the frequency domain using a FFT. The size of the FFT (NFFT) should be selected based on the required resolution of the hyperspectral band of interest to optimize for retrieval performance and dc power consumption. As an example, a hyperspectral IF band covering a window channel may need 10–100 MHz hyperspectral channels while sounding near the V-band oxygen would require 0.5–3 MHz channels to match ATMS vertical resolution performance. After conversion to FFT frames (each frame representing NFFT samples), counts are converted to power and integrated over a number of frames equal to the beam period. Finally, hyperspectral bins can be aggregated to form multispectral channels through a weight

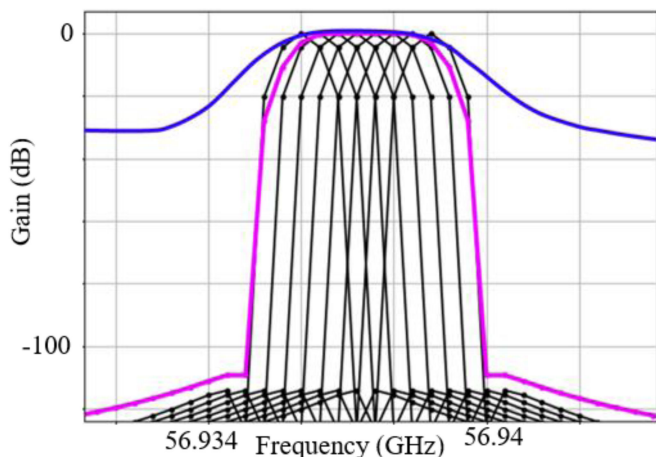


Fig. 3. ATMS channel 15 digital construction. The reconstructed digital channel response (magenta) exceeds ATMS performance (blue) in passband flatness, transition bandwidth, and stopband rejection.

vector dot product. Digital spectral responses are formed by combining FFT bins spanning the bandwidth associated with a target ATMS channel. Bins within the specified passband are assigned a weight of 1.0 while all others are weighted with 0.0. An optimal response has an attenuation-free passband with sharp transition bands and high stopband rejection. An illustration of this technique is shown in Fig. 3. The spectral response function of the digital filter (magenta) is formed through the combination of eight adjacent bins (black) with nonzero weighting.

Stopband rejection of greater than 100 dB is achieved, which far exceeds the filter performance documented in S-NPP ATMS public spectral response function (SRF). These multispectral products can be continuously digitally calibrated and made to match the format of legacy instruments.

Since 2016, Northrop Grumman Space Systems has been developing a digital hyperspectral radiometer leveraging the architecture described previously. The Digital Backend (DBE) radiometer was designed for use in multiple orbits, payload configurations, and science bands. In 2020, the DBE was used as the reference design for multiple NOAA LEO/GEO studies (NOAA-BAA-LEO-GEO); The Microwave Reference Intercalibration Radiometer, the microwave component of the Microwave Infrared Radio Occultation study, and the Geostationary Microwave Sounding Unit. As shown in Fig. 4, the first DBE prototype CCA with path-to-space components reached TRL-6 through internal R&D in 2020.

The DBE CCA is a self-contained digital spectrometer with on-board voltage regulation, clock generation, analog to digital converter ICs, and processing FPGA. The assembly requires only a 5 V source, programming and communications interfaces, and an RF input. This integrated device enables many different instrument configurations and packaging options to create economies of scale across multiple hyperspectral microwave missions.

The digital backend prototype features two dual-converter ADC macros capable of sampling at 3.125 Gsps per converter. Future generations of the DBE will extend sampling rates to

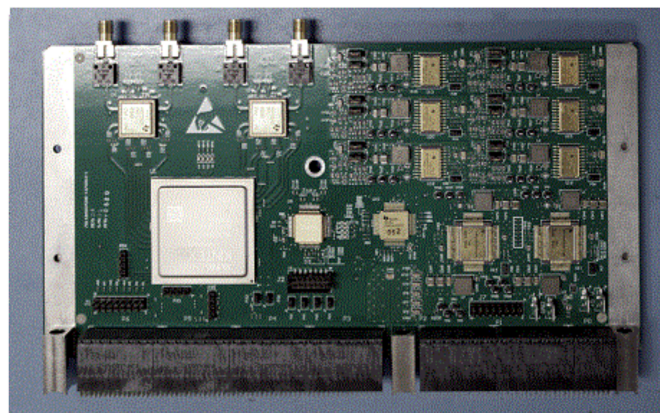


Fig. 4. Northrop Grumman digital backend path-to-space prototype.

5 Gsps per converter. The extended sampling rate and interleaving of multiple converters will provide up to 10 GHz instantaneous bandwidth to the spectrometer processing chain. The ADCs convert a wideband IF signal into 12-bit samples prior to packetization and transmission to the DBE FPGA via 16 HSS transceiver pairs running at 12.5 Gbps. In the FPGA, time series samples are converted to spectral bins, integrated, and hyperspectral channels are aggregated into multispectral bands to form the primary sensor data products to be transmitted by the spacecraft communications downlink.

ATMS covers RF bands from 23 GHz to 193 GHz with a complex receiver architecture. To provide a single digital hyperspectral solution covering the same science bands, a flexible architecture is needed. Purpose built IMAs enable band specific IF selection in low size, weight, and power form factors. IF channels of varied widths require digital backends with multiple sampling options. The DBE CCA allows three possible configurations. In quad-channel mode, the DBE digitally converts four distinct IFs into hyperspectral power spectral density measurements with up to 1.5625 GHz of digital bandwidth. Dual-channel mode offers on-chip interleaving for two hyperspectral bands with 3.125 GHz of bandwidth. Finally, the fully interleaved mode is used to synthesize a single ultrawideband ADC supporting digitization of up to 6.25 GHz of spectrum. On-board interleaving of high speed data converters requires additional design considerations. Subtle difference in gain, offset, and phase between the converters and RF paths can lead to large spurious content in the processed spectrum. When the RF front-end is constructed such that T_{hot} is near ADC saturation, a gain mismatch between sub ADCs of < 1 dB would create an error near the same order of magnitude of the current ATMS NEDT. An interleaving sampling error of 5% has the same effect. DC bias is less problematic as ADCs are usually calibrated to within a few quanta of 0 counts @ 0 volts. RF splitting networks must be carefully matched and a robust thermal solution is required to minimize gradients between components. This mode is reserved for wide bandwidth spectral regions with many science channels of interest (i.e., lower V-band 50–56 GHz). To maintain the performance of the ADCs, the DBE FPGA provides additional

calibration structures that continuously monitor and characterize the primary error sources of interleaved architectures. With maintained interleaving quality, the LNA noise figure will continue to be the driving factor in system noise equivalent differential temperature (NEDT).

Leveraging currently available technologies and following an approach similar to the one detailed in this report, hyperspectral microwave radiometry will become a core part of the next generation of earth observational systems. Continued advancements to component technology and signal processing techniques will ensure that this capability will transition from experimental to part of the operational NWP missions in the near future.

III. BENEFITS AND LIMITATIONS

Hyperspectral soundings, by disaggregating channel information, can provide additional information over legacy radiometers. The focus here is on three distinct benefits—those associated with improved temperature and moisture soundings, those associated with better RFI detection and screening, and those associated with using the sensor as a radiometer intercalibration reference standard. Improved retrievals have been previously examined [3], [4]. Blackwell *et al.* [3] proposed a multiplexer concept and examined a radiometer with 72 channels in the 118 GHz band with an additional 16 channels at 183 GHz. Their results showed roughly a 0.5K improvement in temperature and a relative humidity improvement of roughly 5%. Boukabara and Garrett [4] assumed 330 channels with 100 MHz bandwidth to cover the 50–60 GHz oxygen band and 183 GHz water vapor line. While their study was not tied to any specific sensor architecture, they did show a roughly 1K improvement in the temperature errors and improvements close to a factor of 3 in the total precipitable water when compared to AMSU/MHS. Other studies [5], [6] also considered increased numbers of channels, but focused on optimally selecting the channels with the greatest information content and their subsequent use in data assimilation studies. Most studies also focused on cloud and hydrometeor retrievals in that these also benefit from increased spectral resolution. However, error covariances are not particularly well known for cloud- and precipitation-affected radiances and are not dealt with here.

A. Temperature and Humidity Soundings

This article uses the European Centre for Medium Range Weather Forecasts (ECMWF) Nature Run, known as ECO 1280 [8] with 16 km spatial resolution and 137 vertical layers to simulate both MIRER (1 MHz) and ATMS sensor radiances. These same radiances are also used to assess how well the temperature and humidity profiles can be retrieved from the simulated “observations” after characteristic sensor noise is added. It assumes both sensors are in the existing ATMS orbit and sample the same scenes. The same optimal estimation (OE) technique [9], [10] is used for the inversion for both sensors—thus ensuring that the performance differences are due uniquely to the sensor characteristics and not due to sampling differences or the inversion technique. Only oceanic, clear air scenes are assessed here in order limit the solutions to simple retrievals,

but also the most difficult to improve [4], as the surface and cloud hydrometeors benefit from the increases spectral resolution while being less sensitive to channel noise than temperature and humidity soundings.

While simulations and subsequent inversions are well defined for ATMS, OE is not as straightforward for hyperspectral sensors, as the mathematics become unstable for too many channels. Also, the narrow bandwidths of the hyperspectral channels tend to be noisy if taken individually. Based on current design characteristics, noise, expressed as the NEDT is assumed to be $4.2K/\sqrt{\text{Bandwidth in MHz}}$ in the K-band, $5.44K/\sqrt{\text{MHz}}$ at V-band and $15.K/\sqrt{\text{MHz}}$ at G-band. While different methods to reduce the effective number of channels and their effective noise exist [11], the current study assumes that channels with the same optical depth will be indistinguishable by the algorithm and can, thus, be averaged on input to reduce the effective channel noise. This article chose effective channels based on a narrow increment in optical thickness ($\tau = 0.0014$) at K-band, increasing to $\tau = 0.11$ at V-band and $\tau = 0.37$ at G-band. The optical thickness increment was chosen to provide 200 channels in each band to allow for a retrieval with up to 600 channels. With the abovementioned ranges for optical depth, pseudochannels have between 30 and 300 individual 1 MHz bands, but there is no requirement that these be contiguous. While this reduces the channel noise, the large number of channels (i.e., 200 for each if the three bands), still causes occasional instabilities in the OE retrieval. Further channel reduction is accomplished by sequentially finding the channels with the greatest impact on the retrieval as measured by a number of metrics defined by [12]. The Jacobian (JBN), degrees of freedom for signal (DFS), and entropy reduction (ER) criteria for assessing channel impact as discussed in [12] were tested with the DFS criteria offering the best overall results. Once the most impactful channel is selected, the process is repeated, until a total of 120 channels were selected. Each impact criteria has its own sequence of most-to-least-impactful channels. When not otherwise specified, the DFS criteria is used in this article.

The OE solution is well described in [9] and [10], some details are application specific. The current algorithm is designed to retrieve the sea surface temperature and surface wind speed along with temperature and specific humidity in 11 atmospheric levels at 1008, 955, 825, 595, 369, 216, 119, 61, 26, 8, 1.2 mb. This was done to allow for meaningful comparisons to ATMS. The initial guess was constructed from the climatology of the abovementioned parameters from ECO 1280 for polar regions (−90 to −60), southern midlatitude regions (−60 to −30), tropical regions (−30 to 30), northern midlatitude regions (30 to 60), northern polar regions (60 to 90). The correlation among temperature and humidity at each layer and the corresponding error covariance matrices were also developed from the ECO 1280 model, using March of 2020 for each region.

B. Results

The first experiment was to run the OE algorithm with the ATMS channels in order to compare to a hyperspectral sensor using 22, 30, 40, 50, 60, 80, 100, and 120 channels. Because

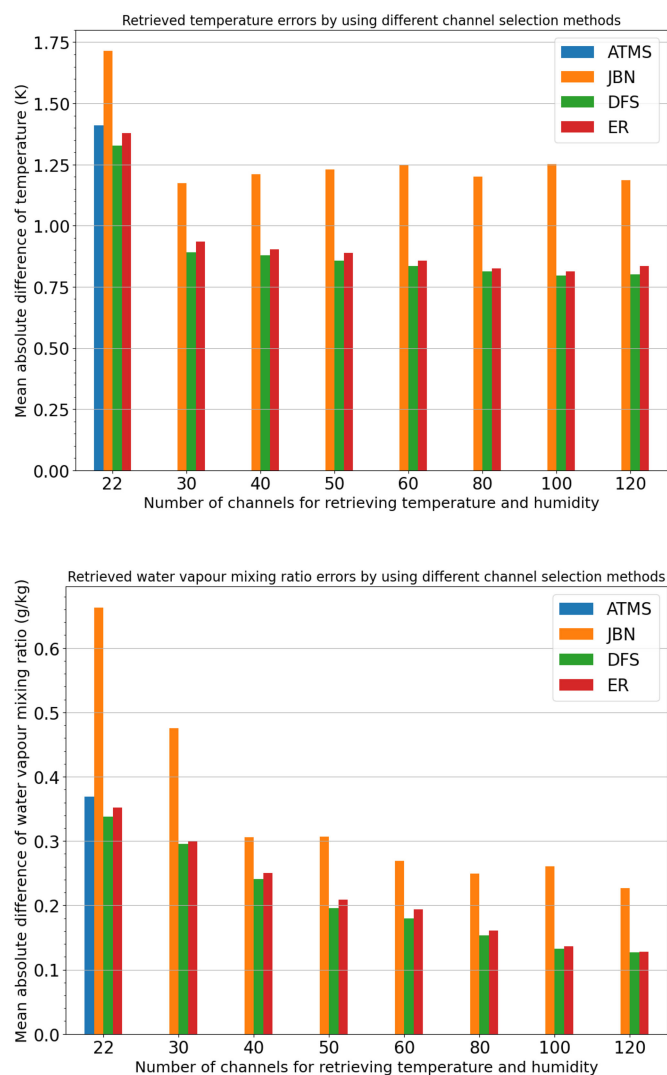


Fig. 5. Mean absolute error in air temperature (top) and water vapor mixing ratio profiles (bottom) from ATMS versus hyperspectral sensor as a function of the channel election criteria and total number of channels. JBN uses a Jacobian based channel selection algorithm, DFS uses the degrees of freedom for signal based channel selection algorithm, and ER uses an entropy reduction based channel selection algorithm.

the brightness temperatures (T_b) are simulated from the ECO 1280 nature run, the true temperature and water vapor mixing ratio profiles are known. Results depicting the mean absolute errors are shown in Fig. 5. Mean absolute error is shown, but root-mean-square errors show the same trend.

The best results in this article were found using the DFS optimization method using around 100–120 channels, although the improvement past 60 channels is only appreciable for the water vapor mixing ratio. Table I summarizes the retrieval error statistics between ATMS and a 120 channel Hyperspectral Microwave Sensor (HyMS). Unlike Fig. 5, root-mean-squared values are presented for easier comparisons with published results. The mean error statistics in Table I for temperature and water vapor mixing ratio were computed using 2000 clear profiles and the DFS method for selecting channels. The temperature retrievals were improved by roughly 0.5K and humidity by roughly 25–50% appears commensurate or slightly better

than previous studies in clear air regions. The improvement in temperature retrievals by roughly 0.5K and humidity by roughly 25–50% appears commensurate or slightly better than previous studies in clear air regions.

A noteworthy result from Fig. 5 is that the Hyperspectral retrieval seems to perform slightly worse than ATMS for each of the three approaches when only 22 channels are used. This is simply due to the selection of effective channels by optical depth. Some regions of the spectrum with few features (i.e., absorption lines) can be aggregated further to reduce sensor noise, but the algorithm was not optimized in this way. Instead, this article aimed to demonstrate the benefits of hyperspectral channels without imposing a limit on the number of channels that the algorithm could select. Beyond that, it is perhaps not surprising that the water vapor retrievals are improved more than the temperature retrievals given that ATMS dedicates 13 channels to temperature soundings but only 5 to humidity sounding. The extra channels, while not revolutionizing the sensor capabilities, nonetheless appear to improve the quality of the moisture retrievals quite significantly.

It is also instructive to compare the channels selected for a 22-channel Hyperspectral retrieval with the DFS channel prioritization to ATMS. These results are shown in Table II. While the channels are not completely different, the Hyperspectral retrieval selected more lines in the water vapor band than ATMS—presumably making use of correlations between water vapor and temperature to improve the low-level temperature as well as humidity (see Table I). Such information can be useful if the ATMS design were to be reexamined, particularly if more channels were contemplated in the future as opposed to a full hyperspectral design.

C. RFI Identification and Mitigation

Traditional sensors such as ATMS have no direct method for detecting RFI beyond testing for nonconvergence of the OE algorithms, or quality control steps in data assimilation, which discards pixels whose brightness temperature differs excessively from the model predicted temperatures. For observational studies, the latter is not a valid reason to reject pixels as poor agreement can result from bad measurements or models. As a result, the failure of convergence of an OE method is often the only quantitative signal that the pixel T_b are not physically consistent with any realistic atmosphere. This tends to occur when a significant amount of RFI contamination is present, but not necessarily with more subtle contamination, which can still impact the quality of the retrieval. In order to examine this further, simulated ATMS radiances (as in the previous section) are used, but with RFI added to the 23.8 GHz channel to simulate potential 5G interference once the 24 GHz band is more widely used. Table III provides the errors that are introduced by various levels of RFI, along with the convergence criteria used to eliminate nonphysical pixels in the OE. The temperature and water vapor mixing ratio deviations from the true value are shown along with their respective retrieval uncertainties. Only with 20K of RFI does the algorithm begin to not converge (98.61%) routinely. With 40K of noise, convergence occurs for only 25.6%

TABLE I
ATMS AND HYPERSPECTRAL MICROWAVE SENSOR ERRORS USING A 120 CHANNEL OE RETRIEVAL (DFS CHANNEL SELECTION)

Pressure (mb)	ATMS T (K)	HyMS120 T (K)	ATMS WV (g/kg)	HyMS120 WV (g/kg)
1000	1.68116	1.27445	1.34323	0.77673
950	1.59688	0.91687	0.89179	0.78021
900	1.73367	0.96062	1.13993	0.92853
850	1.38992	1.00533	1.20963	1.13027
800	1.83782	1.46236	1.27823	1.05162
750	2.04842	1.41491	1.11439	0.77624
700	1.90410	1.25222	0.89294	0.66046
650	1.41407	1.00889	0.92116	0.74453
600	1.35359	0.87261	0.98156	0.58680
550	1.20790	0.93267	0.93961	0.63538
500	1.29566	1.00016	0.69500	0.45315
450	1.32490	1.12227	0.48783	0.32048
400	1.41695	1.24417	0.43064	0.24084
350	1.39526	1.10472	0.29755	0.12099
300	1.68609	1.19591	0.13115	0.06508
250	2.02535	1.59122	0.04678	0.03303
200	1.98434	1.73359	0.01211	0.00981
150	1.37310	1.36221	0.00869	0.00203
100	4.10830	1.61665	0.00063	0.00043
50	1.54735	1.29133	0.00034	0.00030

TABLE II
ATMS AND HYPERSPECTRAL EFFECTIVE CHANNELS SELECTED BY THE CHANNEL SELECTION METHOD BASED ON THE DFS OPTIMIZATION

Channel	ATMS		Hyper-Spectral Sensor (DSF)	
	Frequency (GHz)	NEDT (K)	Frequency (GHz)	NEDT (K)
1	23.8	0.5	22.379	0.374
2	31.4	0.6	25.963	0.828
3	50.3	0.7	50.236	0.25
4	51.76	0.5	50.853	0.21
5	52.8	0.5	52.107	0.34
6	53.596±0.115	0.5	52.338	0.4
7	54.4	0.5	54.474	1.09
8	54.94	0.5	54.653	0.52
9	55.5	0.5	55.194	0.64
10	57.290344	0.75	56.231	0.63
11	57.290344±0.217	1.0	56.348	0.56
12	57.290344±0.3222±0.048	1.0	56.965	0.94
13	57.290344±0.3222±0.022	1.5	56.967	1.38
14	57.290344±0.3222±0.010	2.2	57.598	0.78
15	57.290344±0.3222±0.0045	3.6	57.601	0.77
16	88.2	0.3	57.612	1.5
17	165.5	0.6	57.613	1.68
18	183.31±7	0.8	150.58	0.44
19	183.31±4.5	0.8	157.37	0.38
20	183.31±3	0.8	171.8	0.52
21	183.31±1.8	0.8	183.16	2.34
22	183.31±1	0.9	183.3	2.25

TABLE III
SUMMARY OF THE COMBINED TEMPERATURE/WATER VAPOR RETRIEVAL PERFORMANCE FROM OE AND HYPERSPECTRAL METHODS

Chan. I RFI [K]	Abs. Mean T Error [K]	T Error due to RFI [K]	SD Error [K]	SD Error due to RFI [K]	OE Convergence [%]	HyMS RFI Detection (TNR) 25% bandwidth affected by RFI	HyMS RFI Detection (TNR) 50% bandwidth affected by RFI	HyMS RFI Detection (TNR) 100% bandwidth affected by RFI
0	1.748	n/a	2.496	n/a	100%	n/a	n/a	n/a
0.1	1.744	0.004	2.494	0.002	100%	87.7%	87.6%	87.5%
0.5	1.732	0.016	2.487	0.009	100%	88.1%	86.0%	88.1%
1.0	1.723	0.025	2.482	0.014	100%	99.4%	88.1%	86.0%
2.0	1.728	0.020	2.482	0.014	100%	99.9%	99.4%	88.1%
4.0	1.829	0.081	2.528	0.032	100%	> 99.9%	99.9%	96.9%
6.0	1.915	0.167	2.638	0.142	100%	> 99.9%	99.9%	99.9%
8.0	2.018	0.270	2.808	0.312	100%	> 99.9%	> 99.9%	99.9%
10.0	2.546	0.798	3.034	0.538	100%	> 99.9%	> 99.9%	99.9%
20.0	4.273	2.525	4.739	2.243	98.61%	> 99.9%	> 99.9%	> 99.9%
30.0	6.872	5.124	7.644	5.148	58.92%	> 99.9%	> 99.9%	> 99.9%
40.0	10.203	8.455	11.744	9.248	25.62%	> 99.9%	> 99.9%	> 99.9%
50.0	12.590	10.842	14.494	11.988	15.10%	> 99.9%	> 99.9%	> 99.9%

TABLE IV
RFI DETECTION RESULTS FOR 22–60 GHz AS A FUNCTION OF ASSUMED RFI SURFACE NOISE VALUES OF 10, 5, 4, 3, 2, 1, 0.5, 0.4, 0.2, AND 0.1K USING A 10 MHz SAMPLING INTERVAL THAT EXTENDS TO COVER THE ENTIRE ATMS CHANNEL 1 BANDWIDTH

RFI Intensity (K)	ETS	Accuracy	TNR
10.0 K	0.246	0.970	0.999
5.0 K	0.273	0.964	0.999
4.0 K	0.165	0.958	0.994
3.0 K	0.166	0.935	0.969
2.0 K	0.082	0.856	0.881
1.0 K	0.045	0.836	0.860
0.5 K	0.041	0.850	0.881
0.4 K	0.012	0.850	0.877
0.2 K	0.005	0.849	0.876
0.1 K	0.001	0.840	0.875

of the cases. Also shown are the absolute and mean-square-errors for temperature and water vapor mixing ratio of the pixels that do converge. The errors can be seen to grow with the added noise even when the OE appears to converge. For 4K noise, the average mean error in the temperature grows by 4.6% (1.829K versus 1.748K) while the mean error increases by 6.4% (0.347 g/kg versus 0.326 g/kg) for the water vapor mixing ratio. The standard deviations increase correspondingly. Table III also shows metrics for the Hyperspectral detection of RFI, which is discussed next. The relevant metric, true negative rate (TNR), represents the percentage of time that HyMS is able to detect the true negative rate or the absence of RFI when the algorithm fails to detect it. At the 1K RFI level, for instance, the algorithm fails

to detect the RFI in 11.9% of the time if RFI covers the entire bandwidth of the 23.8 GHz channel, but the failure rate reduces to 3.1% if the RFI signal increases to 4K.

The RFI interference algorithm for the hyperspectral sensor is based on the natural correlation between nearby channels in uncontaminated fields of view. The RFI detection algorithm was built by developing correlation matrices between channels in the physical atmosphere (i.e., w/o interference). Because of noise in the hyperspectral sensor and for computational expediency, 10 MHz channels with appropriate NEDT (i.e., 1.3K at K band) were used to create the correlation matrices using 1 month of the ECMWF Nature Run data. When RFI is added, the correlations break down. Therefore, an algorithm was created (and tuned) to detect the breakdown in these natural correlations. This is known as the weighted average RFI detector. The algorithm does not assume any *a priori* RFI conditions, but rather cross checks for expected correlations between all relevant channel combinations. If the observed correlation is below the threshold set for expected correlations, the channel is marked as having possible contamination.

While there are many different metrics to report success in detecting RFI, the focus here is on three such metrics. The simplest one is the accuracy. Metrics traditionally use 2×2 contingency tables of possible prediction outcomes (RFI/No RFI in our case). The table consists of correct detection of RFI a), detection of RFI when none is present b), RFI is present but not detected c), and no RFI is correctly detected d). The Accuracy metric simply reports on the fraction of correct predictions (a) + (d) in the abovementioned nomenclature

$$\text{Accuracy} = \frac{a + d}{a + b + c + d} \quad (1)$$

While accuracy is easy to interpret when positive and negative outcomes are equally likely, it can give distorted views when one

outcome is much more likely than another. If RFI is a rare event, for instance, then always predicting “no RFI” will give a good accuracy score despite the lack of real skill. To overcome this potential distortion, the equitable threat score (ETS) is used as it provides universal skill in predicting binary events (RFI/No RFI in our case) that account for chance predictions. Using the same 2×2 contingency tables and nomenclature defined previously, the ETS is defined as [13]

$$\text{ETS} = \frac{a - \text{chance}}{a - \text{chance} + b + c} \quad (2)$$

where

$$\text{chance} = \frac{(a + b)(a + c)}{a + b + c + d}. \quad (3)$$

ETS is also known as the Gilbert skill score [13] or the “bias-removed” threat score [14]. In practice, ETS represents the fraction of correctly predicted observational events, adjusted for the associated random chance of being correct, [15], [16]. A perfect ETS is 1.0, no skill is 0, and $-1/3$ is the lower bound (a perfectly bad model that has the opposite forecast condition all the time). This makes it a more suitable metric for when RFI ranges from low to high without biasing the results based upon the particular RFI probability distribution [17].

A final metric used here is the TNR, which is simply $(d)/(c)+(d)$. This metric is useful in fields such as data assimilation, which is willing to aggressively screen data to ensure that RFI-contaminated pixels are not introduced into the assimilation.

Table IV presents the results for these three metrics as a function of the RFI signal strength. The RFI is assumed to cover the entire ATMS Channel 1 bandwidth in these examples.

In general, the pattern indicates that the negative conditions get harder to detect as the RFI approaches the instrument noise value (1K) and more brightness temperatures are falsely labeled as RFI-contaminated. As expected, the result shows that with lower (and harder to detect) RFI intensity, the accuracy and ETS metrics are also lower. However, the relatively high TNR values indicate that there is still substantial skill in detecting clear non-RFI conditions for RFI intensities above the hyperspectral instrument noise at narrow wavelengths. When compared to the TNR performance, the true positive rates (TPR) (not shown) exhibit a stronger decline in performance as the RFI intensity declines (e.g., the TPR is 0.129 at an RFI intensity of 0.1K). As the RFI signal strength declines and becomes obscured by the instrument noise, the low ETS values show that the skill approaches random conditions. It should also be noted that the results shown are for uncorrelated 10 MHz sampled detection instances. If banded RFI transmissions are assumed, the relatively high TNR values could be propagated to adjacent frequencies and improve the overall bandwidth detection accuracies. However, in this case, we merely present the individual sampled detector results and make no assumptions regarding RFI bandwidth correlation.

While the ATMS sensor is only sensitive to the net RFI that it senses in the FOV, hyperspectral sensors are capable of detecting the lack of correlation and the location at which this occurs. For the hyperspectral sensors, both the level of RFI, as well as

the penetration of the RFI into the 23.8 GHz channel are thus important (assuming RFI comes from leakage of 5G transmitters below the agreed-to 24 GHz band). Instead of simply assuming a level of RFI that contaminates the 23.8 GHz channel as was done for ATMS, we consider both the signal strength of the RFI and the level of intrusion into the ATMS band. For example, 25% intrusion assumes the RFI extends from 25 GHz down to 23.87 GHz; 50% refers to the band center of 23.8 GHz, and 100% intrusion assumes the RFI covers the entire ATMS bandwidth down to 23.62 GHz. The RFI signal is assumed flat but drops off by 20 dB per MHz beyond the indicated value.

Table III summarizes the aggregate performance statistics of ATMS temperature and water vapor retrievals for various levels of RFI, along with the capabilities for detecting the indicated RFI through convergence failure (of an OE algorithm). In addition, we present the TNR results for the Hyperspectral RFI detection algorithm using various penetrations of the RFI signal into the ATMS bandwidth. For consistency, a 1K RFI signal in the ATMS footprint corresponds also to 1K signal for the hyperspectral sensor when the entire bandwidth is affected, but a 2K signal if only 50% of the bandwidth is affected by RFI and 4K signal if only 25% of the bandwidth is affected by the interference.

D. Hyperspectral Observations for Intercalibration Reference

If two sensors are identical, intercalibrating them is a straightforward exercise in comparing Tbs when the sensors view the same scene from the same direction. However, difficulties matching view directions and channel response functions, even if the same central frequency is being observed, complicate this simple scenario. To intercalibrate sensors, one generally uses a double difference technique during coincident overpasses of relatively homogeneous scenes. In the double difference technique, the underlying scene (as described by a model reanalysis, or derived from the reference sensor itself), is then used to simulate Tb for the reference sensor and target sensors in order to quantify the expected differences due to differences in channel frequencies and view angles. This expected difference can, then, be subtracted from the observed differences to quantify the calibration error and noise. If the two sensors are identical, and their view angles are matched, then their simulated Tb are, by definition, also identical, and the calibration differences reduces to the observed Tb differences. In practice, however, sensors and view angles are rarely identical.

Uncertainty in the double difference is introduced when slightly incorrect scene descriptions are used to compute the simulated Tb. Errors in the scene description propagate into the simulations and translate into additional noise being assigned to the target sensor. The closer the reference and target sensors are to each other, the smaller the impact of scene errors in the final calibration errors [18]. For this article, because both the “observed” and “simulated” scenes for both reference and target sensors are simulated, they do not contain the typical errors that are encountered in practice from imperfect scene descriptions. To account for this, we use ERA5 for “observations” but ERA-Interim of the same scene for “simulations”. Retrieval errors for the nonraining parameters over oceans documented in [9] are

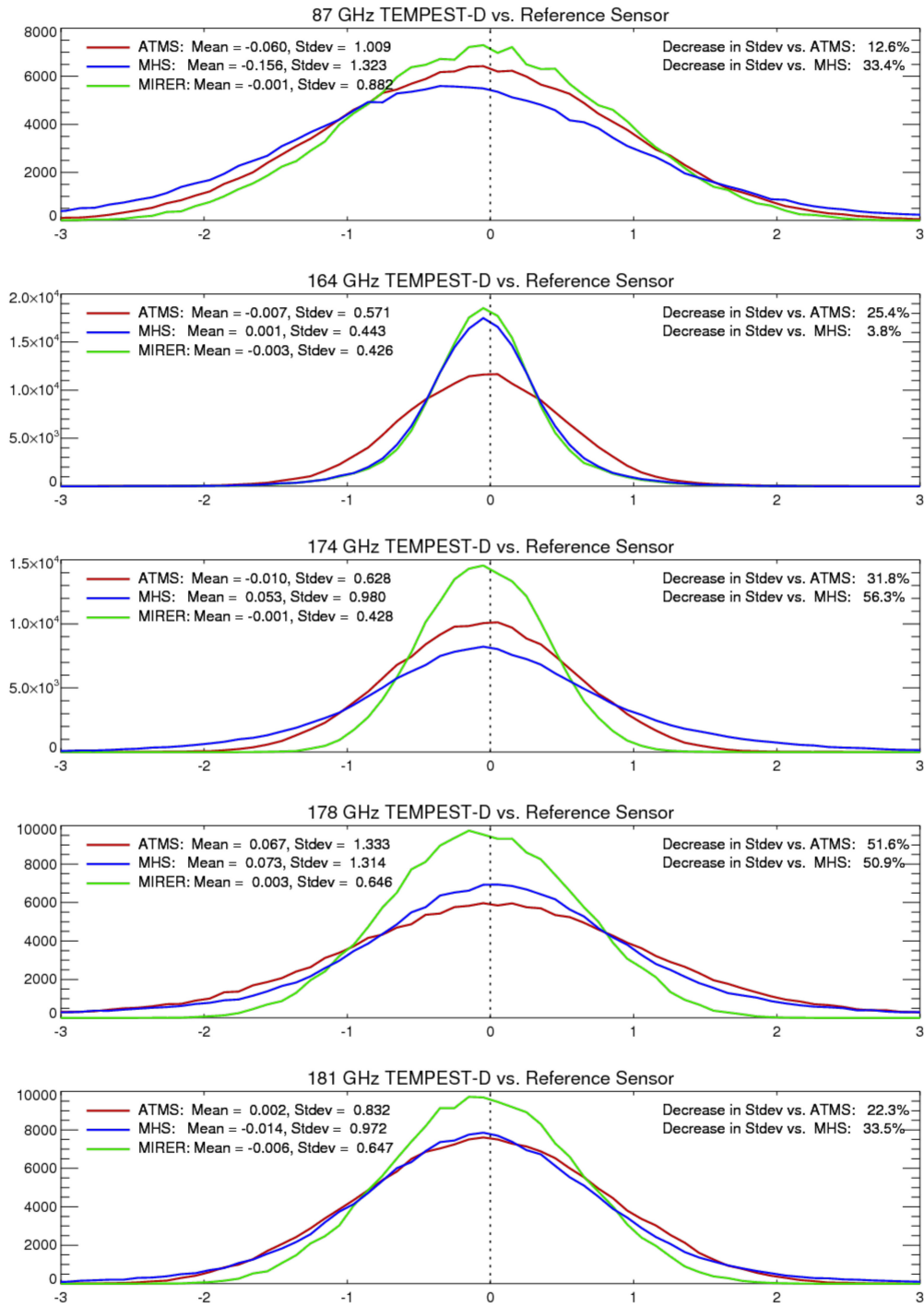


Fig. 6. Plot of histogram of simulated double differences for TEMPEST-D (target sensor) versus three different reference sensors. ATMS (red), MHS (blue), and MIRER (green).

similar in magnitude to the rms difference between ERA-5 and ERA-Interim.

With the abovementioned framework laid out for the double difference method, we compared MIRER’s capabilities for intercalibrating observations from the temporal experiment for storm and tropical systems (TEMPEST) radiometer [19] relative to ATMS and MHS. TEMPEST was chosen as a realistic target radiometer as CubeSats may indeed be used in the future to enhance atmospheric soundings. In all cases, MIRER Tbs are

computed to correspond to the ATMS swath, and actual overpasses between the ATMS and TEMPEST were used. MIRER channel response functions were assumed to match TEMPEST exactly while ATMS and MHS reported channel response functions were used. Only scenes with 20° of nadir, and within ±5° of each sensor were used to minimize the impact of View angle differences. Results are shown in Fig. 6.

What is evident from Fig. 6 is that noise is reduced by MIRER in all 5 channels of TEMPEST, but the degree of improvement

relative to ATMS and MHS varies. This is a direct consequence of the match between the channel differences between ATMS and MHS and their corresponding TEMPEST equivalent. Where the channel pairs are close, ATMS or MHS performance is closer to MIRER. Where the channels are wider apart, the MIRER advantage is more pronounced. For future radiometers, whose exact nature is unknown, the advantage of a MIRER-type response is, thus, essential to narrow the root-mean-square differences.

IV. SUMMARY

With hyperspectral, or fine spectral resolution microwave sounders now viable as replacements to the current operational microwave sounding instruments, this article explores some of the benefits that such a system might provide. While perhaps predictable, this article demonstrates that retrievals of temperature and moisture soundings can be improved by as much as 50% when 60–80 appropriately chosen pseudochannels are employed. While the current simulations were limited to cloud free oceans, perhaps even greater benefits can be realized over land and cloud conditions where additional channels can help constrain the surface and clouds. It should be noted that the OE retrieval with hyperspectral sensors is computationally slow as the optimal channel set must be found for each pixel. However, it is easy to envision a scenario under which the full inversion is used only to train a neural network schemes that can reproduce the detailed calculation fast enough for operational applications.

The article also showed the significant advantages of hyperspectral sensors as a way to detect RFI. While the work did not focus on mitigation strategies, the need to detect the RFI, and eliminate those pixels from further analysis is essential for both climate data records and data assimilation. More work, with specific RFI patterns would need to be conducted before statements could be made about mitigation.

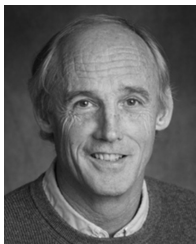
Finally, hyperspectral sensors, through their ability to dynamically adapt their frequency response function to any other orbiting microwave sounder, can play a crucial role in reducing calibration differences and uncertainties among sensors. By itself, this would be a valuable asset for the NWP community that relies on assimilating ever more passive microwave sensors.

ACKNOWLEDGMENT

The authors would like to thank ECMWF for producing and CIRA/CSU for distributing the T1279 ECMWF Nature Run.

REFERENCES

- [1] S. B. Healy and J.-N. Thépaut, "Assimilation experiments with CHAMP GPS radio occultation measurements," *Quart. J. Roy. Meteorol. Soc.*, vol. 132, no. 615, pp. 605–623, Jan. 2006, doi: [10.1256/qj.04.182](https://doi.org/10.1256/qj.04.182).
- [2] C. Lupu, A. Geer, T. McNally, and C. Crdinali, "Data assimilation diagnostics: Assessing the observations impact in the forecast," *ECMWF Data Assimilation Training Course*, Mar. 29, 2017.
- [3] W. J. Blackwell *et al.*, "Hyperspectral microwave atmospheric sounding," *IEEE Trans. Geosci. Remote Sens.*, vol. 49, no. 1, pp. 128–142, Jan. 2011.
- [4] S. Boukabara and K. Garrett, "Benefits of a hyperspectral microwave sensor," in *Proc. SENSORS*, 2011, pp. 1881–1884, doi: [10.1109/ICSENS.2011.6127357](https://doi.org/10.1109/ICSENS.2011.6127357).
- [5] J.-F. Mahfouf, C. Birman, F. Aires, C. Prigent, E. Orlandi, and M. Milz, "Information content on temperature and water vapour from a hyper-spectral microwave sensor" *Quart. J. Roy. Meteorol. Soc.*, vol. 141, no. 693, pp. 3268–3284, Oct. 2015, doi: [10.1002/qj.2608](https://doi.org/10.1002/qj.2608).
- [6] F. Aires, C. Prigent, S. A. Buehler, P. Eriksson, M. Milz, and S. Crewell, "Towards more realistic hypotheses for the information content analysis of cloudy/precipitating situations – application to a hyperspectral instrument in the microwave," *Quart. J. Roy. Meteorol. Soc.*, vol. 145, no. 718, pp. 1–14, 2019.
- [7] J. R. Piepmeier *et al.*, "Radio-frequency interference mitigation for the soil moisture active passive microwave radiometer," *IEEE Trans. Geosci. Remote Sens.*, vol. 52, no. 1, pp. 761–775, Jan. 2014, doi: [10.1109/TGRS.2013.2281266](https://doi.org/10.1109/TGRS.2013.2281266).
- [8] R. N. Hoffman, S. Malardel, and T. Peevey, "New 14-month forecast available for research" ECMWF Newsletter No. 158, Jan. 2019. [Online]. Available: <https://www.ecmwf.int/en/newsletter/158/news/new-14-month-forecast-available-research>
- [9] D. I. Duncan and C. D. Kummerow, "A 1DVAR retrieval applied to GMI: Algorithm description, validation, and sensitivities," *J. Geophys. Res. Atmos.*, vol. 121, no. 12, pp. 7415–7429, Jun. 2016, doi: [10.1002/2016JD024808](https://doi.org/10.1002/2016JD024808).
- [10] R. M. Schulte and C. D. Kummerow, "An optimal estimation retrieval algorithm for microwave humidity sounding channels with minimal scan position bias," *J. Atmos. Ocean. Technol.*, vol. 36, no. 3, pp. 409–425, Mar. 2019, doi: [10.1175/JTECH-D-18-0133.1](https://doi.org/10.1175/JTECH-D-18-0133.1).
- [11] F. Aires, V. Pellet, C. Prigent, and J.-L. Moncet, "Dimension reduction of satellite observations for remote sensing. Part 1: A comparison of compression, channel selection and bottleneck channel approaches," *Quart. J. Roy. Meteorol. Soc.*, vol. 142, no. 700, pp. 2658–2669, Oct. 2016, doi: [10.1002/qj.2855](https://doi.org/10.1002/qj.2855).
- [12] F. Aires *et al.*, "Microwave hyperspectral measurements for temperature and humidity atmospheric profiling from satellite: The clear-sky case," *J. Geophys. Res. Atmos.*, vol. 120, no. 21, pp. 11334–11351, Nov. 2015, doi: [10.1002/2015JD023331](https://doi.org/10.1002/2015JD023331).
- [13] D. S. Wilks, *Statistical Methods in the Atmospheric Sciences: An Introduction*. San Diego, MA, USA: Academic, 1995.
- [14] D. R. Novak *et al.*, "Precipitation and temperature forecast performance at the weather prediction center," *Weather Forecast.*, vol. 29, no. 3, pp. 489–504, Jun. 2014, doi: [10.1175/WAF-D-13-00066.1](https://doi.org/10.1175/WAF-D-13-00066.1).
- [15] A. J. Clark, W. A. Gallus, and M. L. Weisman, "Neighborhood-based verification of precipitation forecasts from convection-allowing NCAR WRF model simulations and the operational NAM," *Weather Forecasting*, vol. 25, no. 5, pp. 1495–1509, Oct. 2010, doi: [10.1175/2010WAF2222404.1](https://doi.org/10.1175/2010WAF2222404.1).
- [16] K. J. Tobin and M. E. Bennett, "Validation of satellite precipitation adjustment methodology from seven basins in the continental United States," *J. Amer. Water Resour. Assoc.*, vol. 48, no. 2, pp. 221–234, Apr. 2012, doi: [10.1111/j.1752-1688.2011.00604.x](https://doi.org/10.1111/j.1752-1688.2011.00604.x).
- [17] A. S. Jones *et al.*, "Use of predictive weather uncertainties in an irrigation scheduling tool Part I: A review of metrics and adjoint methods," *J. Amer. Water Resour. Assoc.*, vol. 56, no. 2, pp. 187–200, Apr. 2020, doi: [10.1111/1752-1688.12810](https://doi.org/10.1111/1752-1688.12810).
- [18] W. Berg *et al.*, "Calibration and validation of the TEMPEST-D cubesat radiometer," *IEEE Trans. Geosci. Remote Sens.*, vol. 59, no. 6, pp. 4904–4914, Jun. 2021, doi: [10.1109/TGRS.2020.3018999](https://doi.org/10.1109/TGRS.2020.3018999).
- [19] S. C. Reising *et al.*, "Passive microwave atmospheric sounder on a cubesat performing science-quality observations for nearly 2 years: Temporal experiment for storms and tropical systems demonstration (TEMPEST-D) mission," in *Proc. CubeSats SmallSats Remote Sens. IV*, 2020, Art. no. 1150504, doi: [10.1117/12.2570371](https://doi.org/10.1117/12.2570371).



Christian D. Kummerow received the Ph.D. degree in atmospheric physics from the University of Minnesota, Minneapolis, MN, USA, in 1987.

He is currently a Professor with the Department of Atmospheric Science, Colorado State University (CSU), Fort Collins, CO, USA. His expertise is in the remote sensing of water vapor, clouds and precipitation. His focus is toward understanding the global hydrologic cycle and how climate change impacts the availability of water. Before coming to CSU, he was the NASA Project Scientist for the Tropical Rainfall

Measuring Mission. His current research interests include determining global precipitation and its physical characteristics, as shown from space- and ground based sensors.

Dr. Kummerow remains a member of the Joint Precipitation Steering Team that now includes the Global Precipitation Measurement mission, as well as the Advanced Microwave Scanning Radiometer team.



Olivia Jarrett received the B.S. degree in computer engineering from San Diego State University, San Diego, CA, USA, in 2018. She is currently working toward the M.S. degree in computer science from the University of Southern California, Los Angeles, CA, USA.

After joining Northrop Grumman in 2019, she has held roles in embedded software, firmware implementation, and project management within the mmWave Remote Sensing Risk Reduction Internal Research and Development group. Her research interests include embedded software, digital signal processing, and technical leadership.



Joseph C. Poczatek received the B.S. degree in electrical engineering from Marquette University, Milwaukee, WI, USA, in 2013 and the M.S. degree in electrical engineering from Johns Hopkins University, Baltimore, MD, USA, in 2015.

From 2013, he has held multiple research and development roles with Northrop Grumman related to digital system architecture and signal processing. His research interests include machine learning for sensor data processing and multirate digital signal processing architectures for RADAR, mmWave radiometry, and communication systems.

and communication systems.



Scott Almond received the B.S. degree in general engineering from Harvey Mudd College, Claremont, CA, USA, in 2011 and the M.S. degree in aerospace engineering from the University of Texas at Austin, Austin, TX, USA, in 2013.

For the past 7 years he has supported multiple roles, most recently Project Manager, within the mmWave Remote Sensing Risk Reduction Internal Research and Development Group, Northrop Grumman, Azusa, CA. His research interests include mission architecture development and electronics design,

integration, and test.



Wesley Berg received the B.S., M.S., and Ph.D. degrees in aerospace engineering from the University of Colorado, Boulder, CO, USA, in 1988, 1989, and 1993, respectively.

He is currently a Senior Research Scientist with the Department of Atmospheric Science, Colorado State University. He was with the Cooperative Institute for Research in Environmental Science within NOAA's Environmental Research Laboratories. His research interests include satellite remote sensing of precipitation and other hydrologic parameters with a focus on

instrument calibration and the development and analysis of satellite retrievals for long-term climate applications.

Andrew Jones received the B.S. degree in physics from Eastern Illinois University, Charleston, IL, USA, in 1986, and the M.S. and Ph.D. degrees in atmospheric science from Colorado State University, Fort Collins, CO, USA, in 1986 and 1996, respectively.

He is currently a Senior Research Scientist and Fellow of the Cooperative Institute for Research in the Atmosphere, where he is working on satellite data assimilation techniques to retrieve soil moisture properties, the development of cross-sensor data fusion techniques. His research interests include the application of weather and climate data analytics to large scale societal problems such as the integrated food system, phytobiome interactions, and infectious disease propagation.

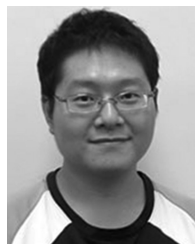
Dr. Jones is a Member of the American Geophysical Union, the American Institute of Physics, and the American Meteorological Society.



Michael Kantner received the B.S. degree in electrical engineering from Rensselaer Polytechnic Institute, Troy, NY, USA, in 1992, and the M.S. and Ph.D. degree in electrical engineering from California Institute of Technology, Pasadena, CA, USA, in 1993 and 1997, respectively.

He was with Northrop Grumman in 2003 and has led a variety of programs and research and development activities, generally focused on the convergence of novel hardware and information processing. Since 2015, he has led the Remote Sensing Systems operating unit, which delivers operational and experimental space sensors for millimeter wave and IR missions.

operating unit, which delivers operational and experimental space sensors for millimeter wave and IR missions.



Chia-Pang Kuo received the B.S. degree in medical imaging and radiological sciences from the Kaohsiung Medical University, Kaohsiung City, Taiwan, in 2007, the M.S. degree in program in remote sensing science and technology from the National Central University, Jhongli City, Taiwan, in 2010, and the Ph.D. degree in atmospheric sciences from the Texas A&M University, College Station, Texas, USA, in 2018.

He was a Postdoctoral Fellow with the Department of Earth, Ocean and Atmospheric Science, Florida State University, Tallahassee, Florida, USA, from 2018 to 2020, on the diurnal cycle of clouds and global energy budget. He is currently a Postdoctoral Fellow with the Colorado State University, Fort Collins, Colorado, USA, focusing on passive microwave retrievals and surface emissivity retrievals.